PCCP

Molecular Magnetism in Nanodomains of Isoreticular MIL-88(Fe)-MOFs

Journal:	*Physical Chemistry Chemical Physics*
Manuscript ID	CP-ART-07-2021-003122.R1
Article Type:	Paper
Date Submitted by the Author:	08-Sep-2021

Complete List of Authors:	Dawood, Sheeba; Joint School of Nanoscience & Nanoengineering, University of North Carolina at Greensboro, Nanoscience Shaji, Surabhi; North Carolina A&T State University, Department of Mechanical Engineering Pathiraja, Gayani; Joint School of Nanoscience & Nanoengineering, University of North Carolina at Greensboro, Nanoscience Mo, Yirong; Joint School of Nanoscience & Nanoengineering, University of North Carolina at Greensboro, Nanoscience Rathnayake, Hemali; Joint School of Nanoscience & Nanoengineering, University of North Carolina at Greensboro, Nanoscience

ARTICLE

Received 00th January 20xx,

Accepted 00th January 20xx

DOI: 10.1039/x0xx00000x

Molecular Magnetism in Nanodomains of Isoreticular MIL-88(Fe)-MOFs

Sheeba Dawood,[a] Surabhi Shaji,[b] Gayani Pathiraja,[a] Yirong Mo,*[a] and Hemali Rathnayake,*[a]

Molecular-based magnetism in nanodomains of three isoreticular MIL-88(Fe) analogues is studied and reported. Microstructures of isoreticular extended frameworks of MIL-88B, MIL-88C, and interpenetrated analogue of MIL-88D, i.e., MIL-126, with the trigonal prismatic **6-c acs** net are synthesized by linking Fe_3O inorganic cluster units with organic carboxylate linkers - benzene-1,4-dicarboxylic acid (BDC), 2,6-naphthalene dicarboxylic acid (NDC), and biphenyl- 4,4'-dicarboxylic acid (BPDC), using a controlled solvent driven self-assembly process followed by a solvothermal method. The powder XRD traces are matched with the simulated diffraction patterns generated from their corresponding crystal structures, revealing the hexagonal symmetry for MIL-88B and MIL-88C, and the tetragonal symmetry for MIL-126. The elemental composition analysis confirms the empirical formula to be $Fe_3O(L)_3$ where L is the organic linker, supporting the formation of isoreticular MIL-88(Fe)-MOFs with the MIL-88 topology. The morphologies of microstructures analyzed by SEM and TEM exhibit long spindle shaped rods with a core and a shell-like architecture for MIL-88B and MIL-88 C whereas MIL-126 shows cubic-shaped microstructures. The M-T plots confirm their blocking temperatures, T_B, to be 60 K, 50 K, and 40 K for MIL-88B, MIL-88C, and MIL-126, respectively. The M-H plots reveal their magnetic response to be ferromagnetic at 10 K with the coercivities, H_C, ranged from 250 G to 180 G. The gradual decreased in the T_B and H_C correlates to the nanocrystals' domain size, which decreases from MIL-88B to MIL-88C to MIL-126. Their phase transition from the ferromagnetic state to the short range ordering of superparamagnetic state is observed at the temperature range of 100 K to 300 K. At $T>T_B$, nanocrystals of all three MIL-88 microstructures act as a single-magnetic domain, owing to their shape anisotropy and finite-dimensionality. The electron density distribution and the spin density state modeled for each MIL-88 analogue exhibit localized electron density and spin density on Fe_3O clusters, indicating that short range magnetic moment ordering in triangular metal oxide nodes with no extended magnetic cooperativity from their organic linkers. The short-range ordering of superparamagnetism in MIL-88(Fe)-MOFs suggests their further study as porous molecular-based magnets.

Introduction

Molecular-based magnetic materials have gained significant attention in the fields of molecular spintronics and quantum technologies due to the ability of tuning their magnetic properties at the molecular level.[1] Replacing conventional inorganic materials and semiconductors, the state-of-the art molecular spintronics aims at developing a new generation of spintronic devices-based on molecular materials.[2] Molecular systems offer exceptionally long-spin relaxation times and enhanced quantum effects in the single-molecule limit, enabling them for integrating into spintronic structures.[3–5] The potential offered by molecules in terms of functionality, performance, and miniaturization for spin-based devices has also motivated the search for novel classes of magnetic molecular materials with multifunctional properties. For example, the development of porous magnetic materials has been a great interest in the past decade because of the intrinsic magnetism and porosity within a single molecular system, which serves as a multifunctional platform for magnetic separation, magnetic molecular sensing, and low-density magnets.[6–9]

Metal-Organic Frameworks (MOFs) are one of the unique families with permanent porosity while offering a vast structural design flexibility to introduce paramagnetic properties via transition metal nodes and magnetic cooperativity, resulting through magnetic exchange via organic linkers with different lengths and functionalities. The porosity of MOFs also offers the possibility of inserting guest molecules into the pores and can use to tune the magnetism of the framework.[10] Specially, within the realm of molecular spintronics, 2D MOFs have recently emerged as molecular-based magnets where single-molecule magnets and spin crossover complexes have been integrated into the nodes of the framework[11–18]. For example, an isomeric Fe^{II}-MOFs exhibits a diamond-like three-dimensional (3D) network spin-crossover to form a rare 2D hard ferromagnet.[11] In another example, long-range ferromagnetism was demonstrated using a Cu-MOF derived from antiferromagnetic dimeric Cu(II) building units and nonmagnetic molecular linkers where copper vacancy had induced the long-range ferromagnetic ordering.[12] However, 3D MOFs have been the recent interest for molecular-based magnets,[19–21] beyond their applications in

[a]*Nanoscience Department, Joint School of Nanoscience and Nanoengineering, University of North Carolina at Greensboro, Greensboro, NC, 27401*
[b]*Department of Mechanical Engineering, North Carolina A&T State University, 1601 East Market Street, Greensboro, NC 27411*

Electronic Supplementary Information (ESI) available: [XPS survey elemental analysis data, TGA graphs, and EDS elemental analysis spectra are included in the supporting information]. See DOI: 10.1039/x0xx00000x

gas storage and separation,[22–24] drug delivery,[25–27] and sensing.[28–31]

3D Magnetic MOFs (MMOFs) built via reticular design principles of the secondary building unit (SBU) approach offer isostructural extended framework with a permanent porosity giving rise to either smart magnetic materials or hybrid materials with synergistic properties.[2,32] Owing to its reticular design at the molecular level, MOFs could offer superior characteristics such as high operating temperature and fascinating multifunctionalities when compared to conventional molecular-based magnets.[2,19,33] There are four ways to incorporate molecular magnetism into the framework using reticular design approaches.[32] The first approach is using isostructural ligands where the denser structures with short linkers can participate in the magnetic cooperativity, inducing long-range magnetic order. The second approach is designing a 3D MOF with first row transition metals (d^4 *to* d^7) where the inorganic cluster nodes have suitable coordination environments to exhibit spin-crossover phenomenon that can arise in response to external stimuli (temperature, pressure, light irradiation, magnetic field, electric field, guest sorption), producing changes in magnetism, color, and structures.[34,35] This framework design approach does not require exchange interactions between neighboring magnetic centers and has no limitations on the length of the ligands, nor the connectivity between the metal centers.[32] The other two pathways are based on designing MOFs with metal nodes, which possess an anisotropic spin-ground state and an isotropic spin-ground state, resulting in single molecule magnet behavior and magnetocaloric effect, respectively.[32]

The work described herein is an example for the synergistic effect of the shape anisotropy, finite-crystal lattice dimensionality, and the isoreticular extended framework on the molecular-based magnetism in 3D microstructures of MIL-88(Fe)-MOFs. Three analogues of MIL-88(Fe)-MOFs; MIL-88B, MIL-88C, and interpenetrated analogue of MIL-88D (i.e., MIL-126) were successfully synthesized by connecting Fe_3O inorganic clusters with three different organic ligands (1,4-benzene dicarboxylic acid (BDC), 2,6-naphthalene dicarboxylic acid (NDC), and 4,4'-biphenyl dicarboxylic acid (BPDC)). A solvent-driven self-assembly followed by solvothermal synthesis method was applied to create 3D-mesoporous microstructures with self-assembled crystalline nanodomains. The structural and chemical compositions, size, shape, crystallinity and packing pattern, and textural properties of microstructures were elucidated to establish the foundation for the understanding of their magnetic response. Magnetic measurements of M-T (Magnetization Vs temperature) and M-H (Magnetization Vs Magnetic field) plots reveal the transitioning of the magnetic response from ferromagnetic at 10 K to short range ordered superparamagnetic at the temperature range of 100 to 300 K, acting self-assembled nanocrystals as single-magnetic domains. The computational analysis conducted for modelling electron density distribution of Fe_3O clusters and spin density state has evidenced that the localized electron density and spin density reside on iron oxide clusters, supporting single-domain molecular magnetism. Owing to the shape anisotropy, finite-size, and the Curie temperature, $\mathbf{T_C}$, above the room temperature, MIL-88(Fe) analogues demonstrate unreported magnetic properties.

Results and discussion

Synthesis and Characterization of MIL-88(Fe)-MOFs: In the past, we have demonstrated a modified solvothermal method to produce crystalline powders of MOFs within 7 to 9 minutes,[36,37] while maintaining their respective topologies as reported for synthetically known MOFs, which have originally synthesized using traditional autoclave-based solvothermal methods.[38,39] Herein, following our previously developed modified solvothermal method, which involves a solvent driven self-assembly followed by a solvothermal process,[37] isoreticular MIL-88(Fe)-MOFs were prepared and their elemental composition, functionality, and crystal structures were elucidated. The XPS survey spectra along with the binding energy spectra corresponding to each element's chemical bonding environments for three MIL-88(Fe)-analogues depicted in **Figure 1** further evidence the successful synthesis of three MIL-88 analogues with di-and trivalent oxidation states of Fe in Fe_3O inorganic clusters. The XPS survey spectra of three MOFs in **Figure 1(a)** confirms the presence of Fe, C, and O with absence of solvent impurities (e.g., DMF) in all three samples. Typically, DMF solvent molecules reside in the pores of MOFs, prepared by the solvothermal process, in which DMF uses as a protic solvent for the deprotonation of the carboxylic acid to make in-situ carboxylate anion.[36,40] The binding energies of Fe 2p obtained for the three MOFs confirm the presence of iron with Fe^{+3} and Fe^{+2} oxidation states from their binding energy peaks at 710 - 711 eV and 723-724 eV, which correspond to Fe^{III} $2p_{3/2}$ and Fe^{III} $2p_{1/2}$,respectively,[21] and their respective satellite peaks at 715 eV for Fe^{+2} without any overlapping between $2p_{3/2}$ and $2p_{½}$.[41] The deconvoluted C 1s spectra of MIL-88 analogues exhibit two binding energies at 283 eV and 286 eV for the chemical bonding states of C-C and O-C=O, respectively, (**Figure 1 (c)**).[42,43] The binding energy at 530 eV for O 1s spectra for all three analogues further confirm the formation of Fe-O-C coordination bonds (**Figure S1**).

As depicted in **Figure 2(a)**, FT-IR spectra of all three Fe-MOFs confirm the formation of the metal-carboxylate coordination framework from the stretching at 1377 cm^{-1}, 1419 cm^{-1}, and 1400 - 1355 cm^{-1} for MIL-88B, MIL-88C, and MIL-126, respectively. The FT-IR spectrum of MIL-88B shows broad hydroxyl stretching around 3400 cm^{-1}, confirming the presence of surface adsorbed water. The elemental analysis of MIL-88B further confirms the presence of water molecules in the sample. Its elemental composition matches to the empirical formula of $Fe_3O(BDC)_3.H_2O$. There are no corresponding hydroxyl stretching observed in the FT-IR spectra of MIL-88C and MIL-126, agreeing with their elemental composition analyses, which confirm MIL-88C's and MIL-126's empirical formula to be $Fe_3O(NDC)_3$ and $Fe_3O(BPDC)_3$, respectively. Thermal stabilities of MIL-88(Fe)-MOFs were analyzed by thermogravimetric analysis (**Figure S2**). All three MIL-88 analogues show three distinct weight losses, initial weight loss of about 10-20% in the temperature range of 100 °C, which could be due to the surface adsorbed moisture in the samples. The second weight loss about 50% is in the

temperature range of 100 – 250 °C, which attributes to the decarboxylation of organic linkers, collapsing the framework. The third weight loss in the temperature range of 300 to 350 °C accounts for the decomposition of the framework, completely. There is a trend in the thermal stability with respect to the organic linker type. The thermal stability increases from 325 °C, 340 °C and 350 °C for MIL-88B to MIL-88C to MIL-126, respectively. Although MIL-126 has higher organic content, it exhibits the highest thermal stability compared to other two due to its rather rigid interpenetrated framework (discussed below).

Crystal structure and topology of MIL-88: The crystallinity, single crystal unit cell structure, and crystal lattice information of MIL-88(Fe)-MOFs were elucidated, and the MIL-88 topology was confirmed, by matching the experimental X-ray powder diffraction traces of synthesized MIL-88(Fe)-MOFs with their simulated powder diffraction patterns. The respective crystallography information retrieved from the Cambridge Crystallography Data Center (CCDC) and Crystallography Open Database (COD) to generate the simulated diffraction patterns. The experimental powder diffraction pattern of MIL-88B shown in **Figure 2(b)** exhibits two well-resolved diffraction peaks at 2θ of 6.89° and 8.89° along with a few minor Braggs peaks at higher 2θ angles and matches with the simulated diffraction pattern generated from the crystal structure of the previously reported MIL-88B (*CCDC 1415803*),[44] The crystal structure of MIL-88B (**Figure 2(c)**) reveals the trigonal prismatic secondary building unit (SBU) attributed to 6-connected ***acs*** net[43] of $[Fe_3(\mu_3\text{-}O)(bdc)_3]$ with hexagonal symmetry that belongs to the space group of P 6_3/mmc. The unit cell constants are a = b = 14.41 Å and c = 17.30 Å, and $\alpha = \beta = 90°$ and $\gamma = 120°$, yielding the unit cell volume of 3114.43 $Å^3$. As depicted in **Figure 2(d)**, the X-ray powder diffraction pattern collected for the synthesized MIL-88C shows four well-resolved but rather broad Braggs peaks, which align well with one of the simulated diffraction patterns of MIL-88C-dry(Fe),[45,46] from three different analogues of MIL-88C(Fe), reported previously.[45–47] The crystal structure of MIL-88C-dry(Fe), shown in **Figure 2(e),** also exhibits 6-connected ***acs*** net of $[Fe_3(\mu_3\text{-}O)(NDC)_3]$ with hexagonal symmetry as MIL-88B, but belongs to P - 6 2 c space group, with cell constants of a = b = 9.90 Å and c = 23.80 Å, and $\alpha = \beta = 90°$ and $\gamma = 120°$, yielding a smaller unit cell volume (2020.12 $Å^3$) compared to the cell volume of MIL-88B. The distance between two Fe_3O clusters within the core in MIL-88B is measured to be 12.00 Å whereas that of in MIL-88C is 13.20 Å, attributing to the increase in the organic linker length.

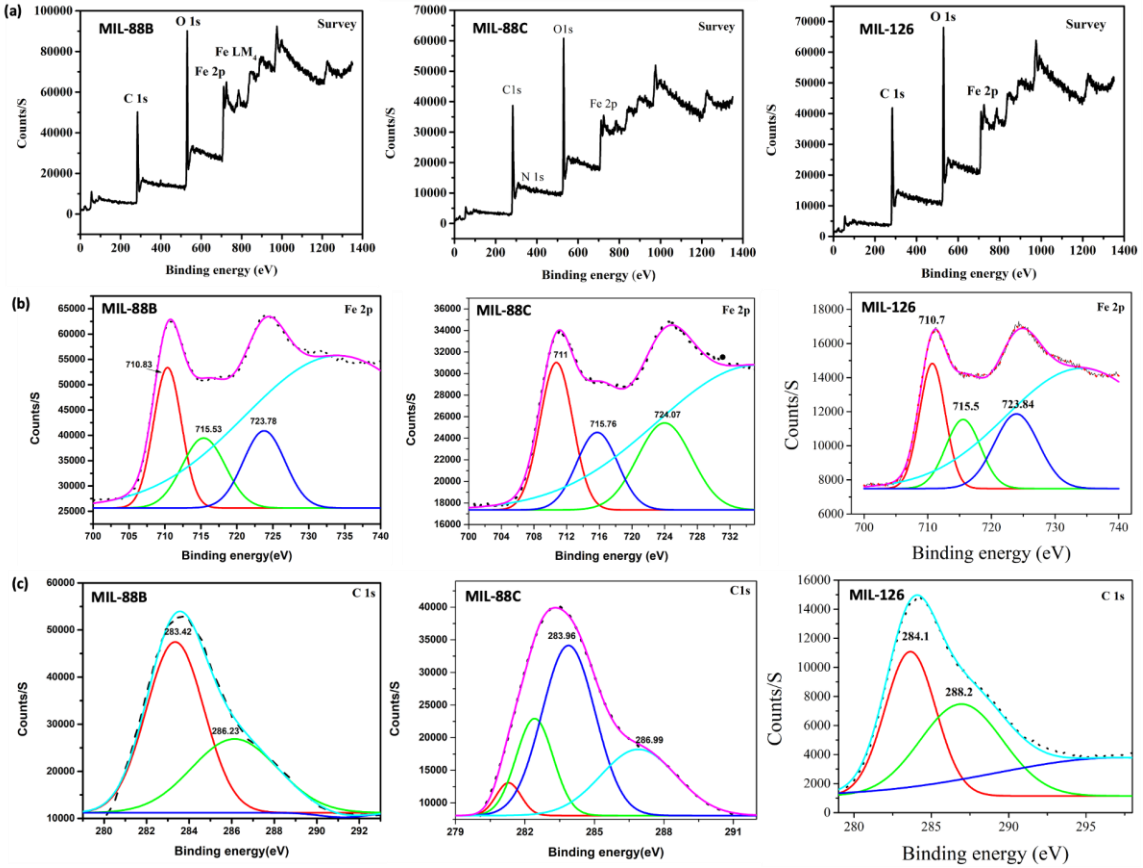

Figure 1. (a) XPS survey spectra; (b) Fe 2P binding energy spectra; and (c) C 1S spectra for MIL-88(Fe)-MOFs.

The powder XRD pattern obtained for synthesized MIL-126 is shown in **Figure 2(f)** and agrees with its respective simulated diffraction pattern generated from the previously reported interpenetrated form of MIL-88D, i.e., MIL-126.[48] The framework of synthetically known MIL-88D exists in two forms, which include non-interpenetrated form (i.e., MIL-88D) and interpenetrated form (i.e., MIL-126). The interpenetrated form belongs to two interwoven ***acs*** nets of class *IIa* (Z=2).[48,49] As shown in **Figure 2(e)**, MIL-126 consists of two interwoven MIL-88D network that belongs to P 4_3 2_1 2 space group. It exhibits a tetragonal symmetry with the longest unit cell lengths of a = b = 21.80 Å and c =

35.40 Å, and $\alpha = \beta = \gamma = 90°$, resulting in the largest unit cell volume of 16826.82 $Å^3$ compared to both MIL-88B and MIL-88C.[49] However, the distance between two neighbouring Fe_3O clusters is 8.93 Å, which is smaller compared to both MIL- 88B and MIL-88C due to the interpenetrated crystal lattice.

BJH Porosity distribution, BET surface area, and Morphology of MIL-88(Fe)-MOFs: The porosity distribution, pore volume, and surface area (S_{BET}) of three MIL-88 analogues with respect to their isoreticular design were evaluated by using BET analysis and BJH N_2 desorption isotherms. The isotherms of MIL-88B, MIL-88C, and MIL-126 (**Figure S3(a)**) show hysteresis between adsorption/desorption curves that resembles type IV category, indicating the capillary condensation which attributes to the mesoporous nature of the materials.[50] A similar type of isotherm was reported previously for MIL-88B(Fe) and α-Fe_2O_3 nanoparticles.[51,52] The characteristic features of Type IV isotherm are associated with its hysteresis loop and in this case the adsorption and desorption isotherms of these MOFs are classified into H3 hysteresis,[51,52] based on IUPAC classification. The BJH pore distributions for MIL-88(Fe)-MOFs (**Figure S3(b)**) and reveals a mesoporous nature with average pore diameters of 5.5, 5.9, and 2.9 nm for MIL-88B, MIL-88C, and MIL-126, respectively.

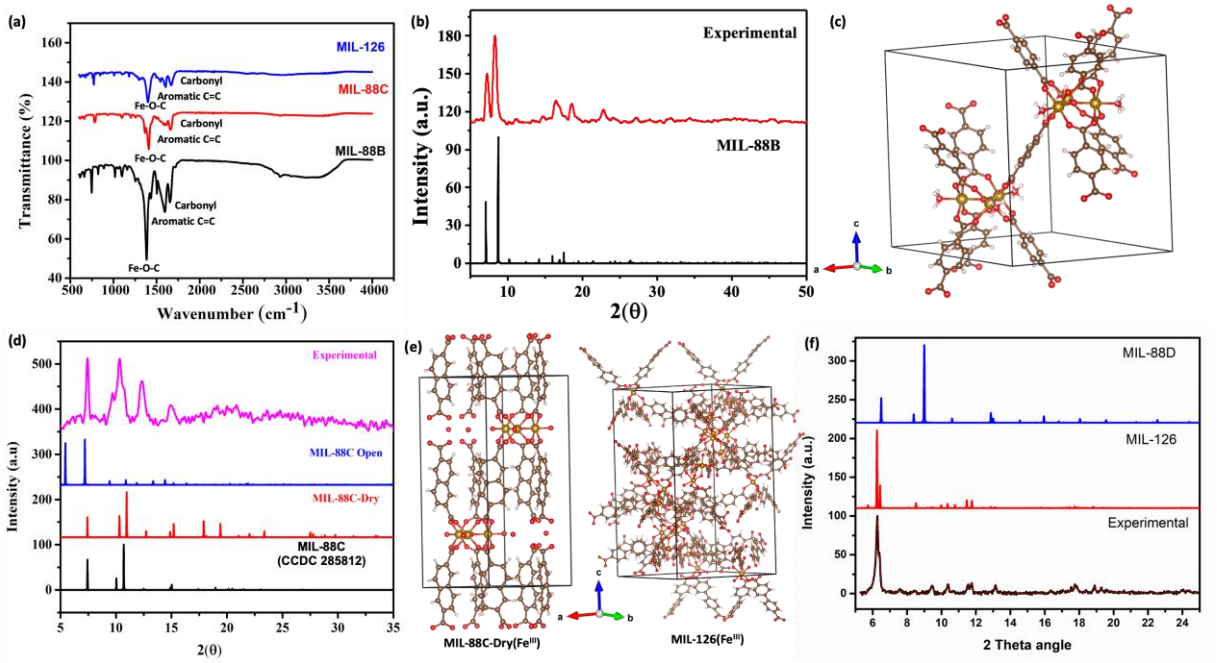

Figure 2. (a) FT-IR spectra of MIL-88(Fe)-MOFs; (b) Experimental and simulated X-ray powder diffraction spectra of MIL-88B; (c) Single crystal unit cell structure of MIL-88B rendered from VESTA using the original cif file of CCDC 1415803; (d) Experimental X-ray powder diffraction pattern of synthesized MIL-88C along with simulated diffraction patterns for three different analogues of MIL-88C reported previously; (e) Single crystal unit cell structures of MIL-88C-Dry(Fe) and MIL-126(Fe) rendered from VESTA using their cif files acquired from the CCDC and COD.[45,46,50]

Table 1 summarizes the S_{BET}, pore volume, and pore size distribution. The S_{BET} and pore volumes of MIL-88B and MIL-88C are considerably lower compared to the S_{BET} and the pore volume of MIL-126, supporting the interpenetrated network with the rigid framework and the largest unit cell volume of MIL-126.[44,46,48] The pore volume of the MIL-88 analogues increases with increasing the length of the linker. In contrast, the average pore diameter is smaller in MIL-126, compared to MIL-88B and MIL-88C due to the formation of two interwoven ***acs*** nets.

Table 1. Textural properties of MIL-88(Fe)-MOFs.

MIL-88 type	S_{BET} (m^2/g)	Total pore volume (cm^3/g)	Average pore diameter (nm)
MIL-88B	91.5	0.13	5.5
MIL88C	95.5	0.14	5.9
MIL-126	693.0	0.44	2.5

Morphologies of MIL-88(Fe)-MOFs microcrystals are investigated by visualizing them using SEM and TEM and are shown in **Figure 3**. The isoreticular modulation of $Fe_3O(CO_2)_3$ SBUs with BDC and NDC linkers has produced microcrystalline rods for MIL-88B and MIL-88C, similar to those reported for Fe-MIL-88B-NH_2 series with BDC-NH_2 organic linkers,[53,54] whereas the SBUs connected with BPDC linkers are self-assembled to produce large-truncated cubes (**Figure 3 (a)**). The HR-TEM images shown in **Figure 3 (b)** for MIL-88B and MIL-88C exhibit unique spindle-like rods with well-tapered edges resembled to nail tips. However, MIL-88C rods are rather thicker with an average diameter of ~400 nm and shorter in length, which ranges from 500 nm to 1µm compared to the spindle rods of MIL-88B. The dimensions of MIL-88B rods are 1-2 µm in length and ~ 200 nm in diameter. The HR-TEM image of MIL-88B rods (an in-set image) reveals the densely packed self-assembled nanocrystals, producing a core like structure (darker contrast) and a lighter contrast periphery with loosely arranged nanocrystals, forming a shell (lighter contrast).

The thicknesses of the core and the shell are found to be ~138 nm and ~47.5 nm for MIL-88B and 169.8 nm and 17.3 nm for MIL-88C, respectively (**Figure S4**).

Comparison to irregular morphologies of MIL-126, previously reported,[55] our solvent driven self-assembly-based solvothermal method produces ordered cubic-shape microstructures for MIL-126 (**Figure 3**). The TEM images of MIL-126 microcrystals, shown in **Figure 3(b)** also reveal the mesoporous nature of cubic microstructures with a rather dense core and lighter periphery. The mesoporous structures are visible in MIL-126 microstructures compared to MIL-88B and MIL-88C morphologies. MIL-126 has produced larger microstructures with a wider polydispersity due to the length of the linker, which can slow the crystallization, producing larger nanocrystals.[56]

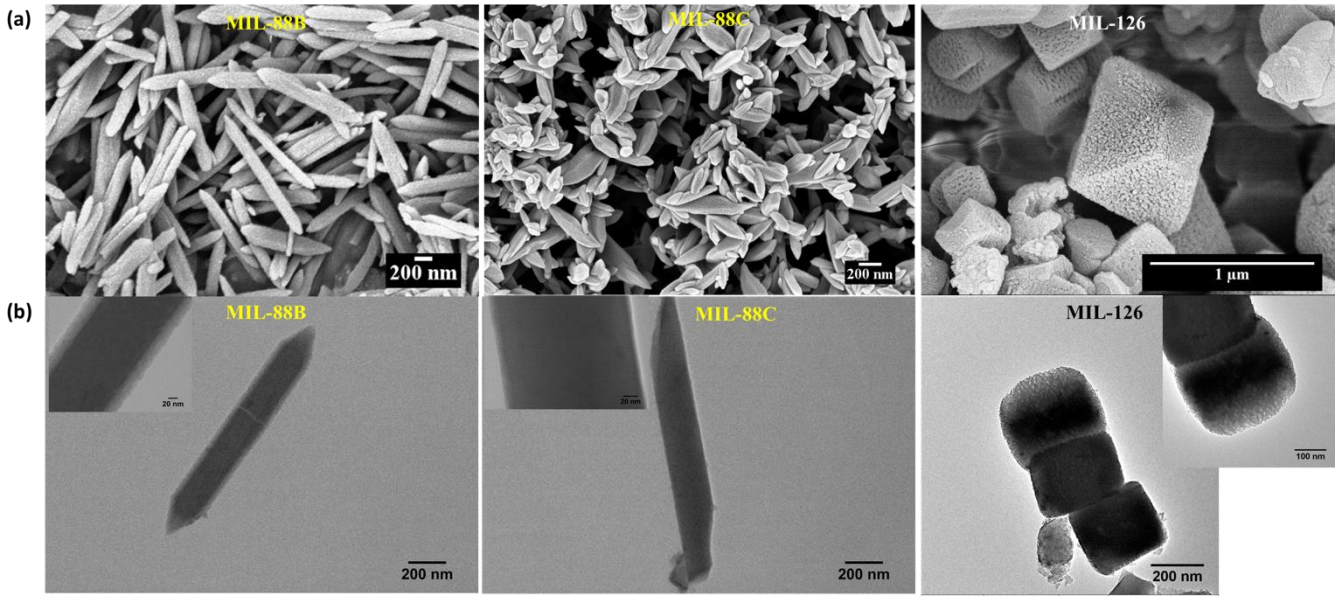

Figure 3. (a) SEM images of MIL-88 (Fe)-MOFs, and (b) HR-TEM images at 200 kV for MIL-88B and MIL-88C and TEM images at 120 kV for MIL-126.

HR-TEM images of single microstructure of each analogue were acquired to confirm whether these microcrystalline structures are self-assembled nanocrystals. For this study, we selected smaller size microcrystals to see intrinsic features better and identify the nanocrystals in each MOF. As shown in **Figure 4**, self-assembled nanocrystals, creating nanodomains, are very visible in the microstructures of MIL-88B and MIL-126 (images taken at 120 kV). The HR-TEM images taken at 200 kV for MIL-88B and MIL-88C further confirm the self-assembled nanocrystals in their microstructures. In MIL-126, nanocrystals are densely packed, but nanodomains of self-assembled nanocrystals are clearly visible with void spaces. The lattice *d*-spacings are estimated to be 3.1 Å, 2.9 Å, and 6.9 Å for MIL-88B, MIL-88C, and MIL-126, respectively, agreeing with the *d*-spacing of their respective diffraction planes of [400], [008], and [310], respectively.

Study of Molecular-based Magnetism in MIL-88(Fe): The magnetic properties of MIL-88(Fe) analogues were studied by acquiring the magnetic data, which include temperature dependence magnetization (M-T), blocking temperature (T_B), and coercivity plots of (M-H) and (M-H/T). Magnetization *verses* temperature (M-T plots) is measured in two different states, i.e., zero-field-cooled (ZFC) and field cooled (FC). The ZFC measurements are used to estimate the blocking temperature (T_B) of each MOF. In a typical ZFC measurements, first, the sample is cooled from room temperature to a particular low temperature in the absence of magnetic field. Then in the presence of a small magnetic field the magnetization is measured as the temperature is being raised. The M-T plots generated in the ZFC and FC measurements can provide qualitative information about the shape anisotropy of the nanocrystals of MOFs and the strength of interaction among Fe_3O clusters in the periodic crystal lattice of MOFs' nanocrystals. For example, if self-assembled nanocrystals of MIL-88(Fe)-MOF act as multi-domains or/and if single-domains are not isolated, the ZFC and FC measurements could produce M-T plots with broader distribution of the blocking temperatures. The size and shape distribution of nanocrystals effects on the blocking temperature of the sample as well. A sample with a wider polydispersity of particles yields a broad peak in M-T curve, in which the blocking temperature cannot be accurately estimated.

The ZFC measurements were conducted by initially cooling the samples from 300 to 10 K in the absence of magnetic field. Then a small magnetic field (200 G) was applied to measure the magnetization as the temperature was being raised. The M-T plots collected in this manner for three MIL-88(Fe)-MOFs are shown in **Figure 5(a)**. All three MIL-88 analogues exhibit an increase in magnetization as the temperature (T) increases, causing the moments to align along the direction of the applied magnetic field by overcoming anisotropy energy and freeing moments from being blocked at $T < T_B$. Typically, if the magnetic clusters are small and single domain, as the temperature increase, the number of these aligned moments increases, reaching a

maximum at T_B, resulting in a peak in the M-T curve.[42,57] The M-T curve collected for each MIL-88 analogue exhibits a noticeable peak, representing T_B for each MOF, and evidence that nanocrystals with Fe_3O clusters in the periodic crystal lattices of each MOF acts as a single magnetic domain, similar to one magnet. Also, as shown in **Figure 5(a**), each MIL-88 analogue exhibits three different blocking temperatures, which decrease from 60 K to 50 K to 40 K for MIL-88B, MIL-88C, and MIL-126, respectively. The decreasing trend in T_B is attributed to increase in nanocrystal size from MIL-88B to MIL-88C to MIL-126. Thus, these results support the reticular expansion by using three different lengths of organic linkers, in which BDC being the shortest linker and BPDC being the longest linker. Therefore, the framework expansion can use to tailor the T_B of MIL-88(Fe)-MOFs while isolating the Fe_3O cluster to act as single magnetic domain.

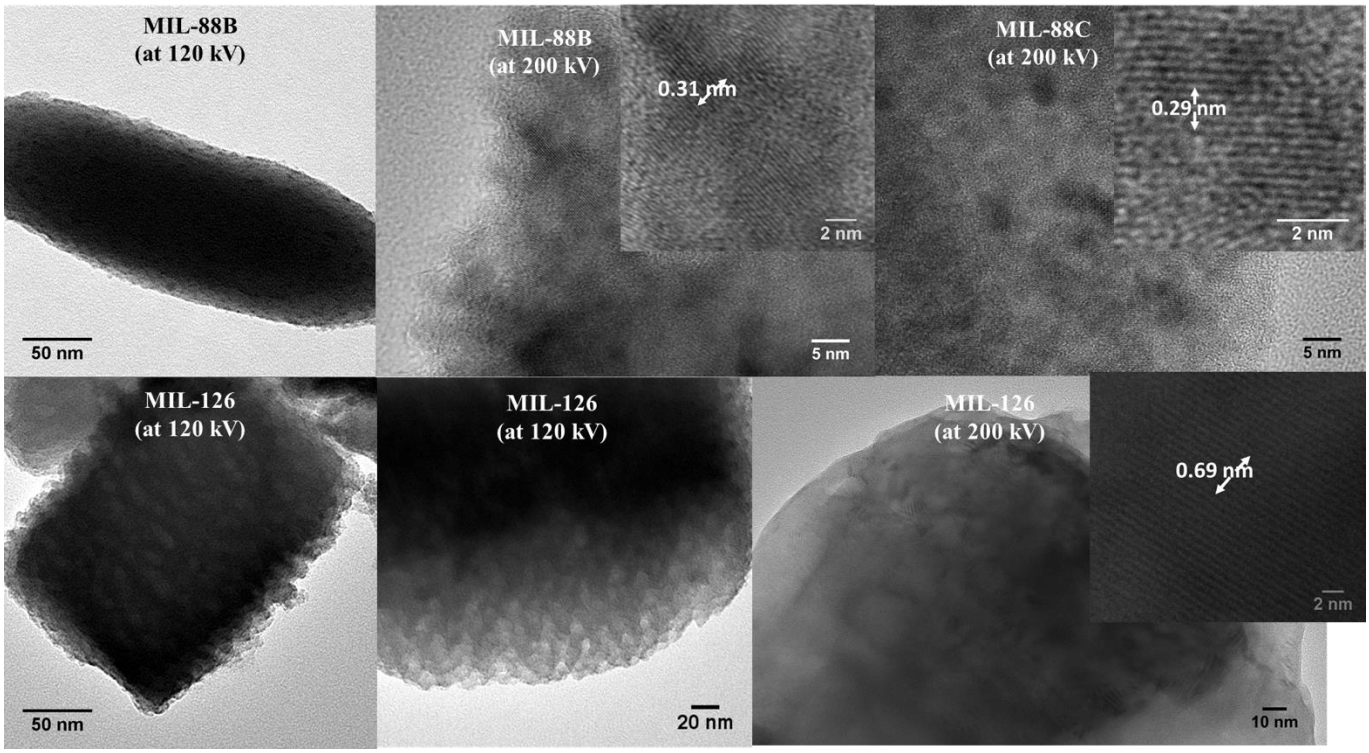

Figure 4.TEM images of a microstructure of MIL-88B, MIL-88C, and MIL-126; In-sets in MIL-88B and MIL-88C images are HR-TEM images with respective lattice d- spacing for nanodomains

In FC measurements, the sample is cooled in a selected temperature range starting from room temperature in the presence of an applied magnetic field. The magnetization is recorded as the temperature is being cooled. From FC measurements, two types of superparamagnetic response can be identified for a ferromagnetic sample. The first type occurs at $T > T_B$, in which the magnetic moments in the particle randomize when the thermal energy becomes large enough. This leads to a very small net magnetization and causes the magnetic moments to flip randomly, resulting in a suppression of the magnetization with an observed net moment of zero for the sample. In such a situation, the sample can display a superparamagnetic behavior above the blocking temperature (*Type I*).[58–60] Another factor needs to be satisfied to observe superparamagnetism at $T>T_B$ is the measuring time (τ_m) being much greater than the Neel relaxation time of the sample (τ_N). In the second type, which occurs at $T<T_B$, thermal energy decreases because of some magnetic moments are becoming smaller than the magnetic moments produced by the aligning field. This causes some moments to align along the field direction, leading to an increase in magnetization. As the temperature decreases further, more and more moments are being frozen along the direction of the applied field. The magnetization of the sample is expected to keep increasing down to the lowest temperature of the experiment. In this case, a system can display a superparamagnetic behavior below a certain blocking temperature (*Type II*), acting as a single molecule-magnet (SMM).[2]

To investigate the magnetic response of MIL-88 analogues at $T<T_B$ and $T>T_B$, coercivity data along with respective hysteresis loops at 10 K and 300 K were collected using the measurement set up described in the experimental section. **Figure 5 (b)-(c)** shows their M-H loops at 10 K and 300 K. Except Fe(II)acetate, the three MOFs exhibit hysteresis loops at 10 K as depicted in **Figure 5(b)**, confirming the ferromagnetic response at $T<T_B$. These M-H plots also reveal the correlation of the coercivity among MIL-88 analogues that characteristics to the nanocrystals' shape and size of each MIL-88. At 10 K, the hysteresis loops exhibit gradual narrowing in coercivity (the loop becoming thinner) from MIL-88B to MIL-88C to MIL-126. (**Figure 5(b) and S5**). MIL-88B with the shortest linker (BDC) exhibits a slightly wider hysteresis loop whereas MIL-126 with the longest

linker (BPDC) has a thinner hysteresis loop, attributing to the increase in nanocrystal size from MIL-88B to MIL-88C to MIL-126. The narrow hysteresis loop in all three MOFs could also characteristics to the separation distance between Fe_3O clusters due to the isoreticular arrangement of the organic linkers in the periodic crystal lattices of nanocrystals in each MOF. The H_C values for MIL-88 analogues are calculated to be 220 G, 210 G, and 180 G for MIL-88B, MIL-88C, and MIL-126, respectively. MIL-88B has the highest H_C, and MIL-126 has the lowest H_C while the H_C of MIL-88C is comparable with MIL-88B. The decreasing trend in the coercivities also reflect the effect of the nanocrystal size and isoreticular nature of each MOF. Thus, the largest H_C value of MIL-88B evidences the collective effect of the linker length and the nanocrystal size on the H_C. For MIL-126, both nanocrystal size and separation between Fe_3O clusters are being larger has resulted the lowest H_C.[61,62]

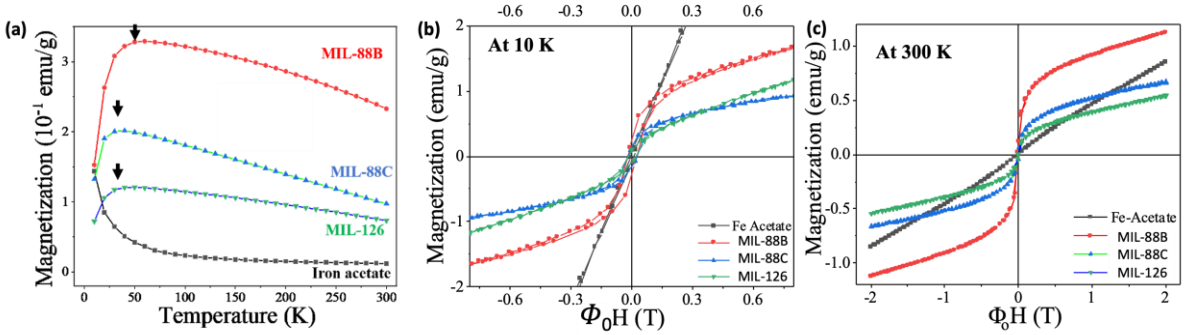

Figure 5. (a) Magnetization *vs* Temperature (M-T) plots for three MIL-88 analogues. The arrows indicate the T_B of each analogue; M-H loops for three MIL-88(Fe) MOFs at (b) 10 K and (c) 300 K

As shown in **Figure 5(c)**, the M-H plots collected for all three MIL-88(Fe)-MOFs at 300 K exhibit no coercivity, but retains the sigmoidal shape of the ferromagnetic response, transitioning to the superparamagnetic response at $T>T_B$ for all three MOFs. The nature of the superparamagnetic response observed here is due to the size of the nanocrystals, which are being at the superparamagnetic size threshold, thereby acting as a single-magnetic domain. It is definitively the size distribution of self-assembled nanocrystals in each MOF are at the superparamagnetic size threshold, i.e., usually <100 nm for ferromagnetic crystals.[63–65] In our case, self-assembled nanocrystals are in the size range of 1-7 nm to 3.5 nm determined from TEM. It is also known that magnetic domains in ferromagnetic crystals with critical size <100 nm cannot split up further into domains, resulting in single domain particles.[63–65] Therefore, it is possible that thermal energy overcomes the magnetic anisotropy energy (E_α), which is usually smaller for smaller particles and causes the thermally activated flipping of magnetic moment on the particle volume, displaying the superparamagnetic behavior at $T>T_B$.[66,67]

The E_α per particle is given by Eq.2:

$E_\alpha = \kappa_{eff} V$ ----------(2); where κ_{eff} is the effective anisotropy constant and V is volume of the particle.

The thermal energy, E_{th} can express at a specific temperature by Eq. 3:

$E_{th} = k_B T$ --------(3); where k_B is the Boltzmann constant and T is the temperature.

Table 1. Nanodomains Dimensions and their anisotropy energy for MIL-88(Fe)-MOFs microstructures

MIL-88 type	Nanocrystals cell length (nm)	Volume (x 10^{-9} m^3)	E_α (x 10^{-5} eV)
MIL-88B	1.7	3.33	3.63
MIL88C	2.3	1.86	2.04
MIL-126	3.5	15.43	16.97

In the current study, we have not conducted temperature dependence coercivity behavior to accurately calculate the effective anisotropy constant for our MOF systems. To roughly estimate the E_α for each MIL-88 analogue, we used the effective anisotropy constant of $FeO.Fe_2O_3$ bulk material and assumed that the effective anisotropy constant of MIL-88(Fe)-MOFs nanocrystals with Fe_3O magnetic domains is comparable to the K_{eff} of $FeO.Fe_2O_3$ (1.1×10^4 J/m^3) at room temperature.[68] The crystal volume for each MIL-88 analogue was obtained from their crystal structures.

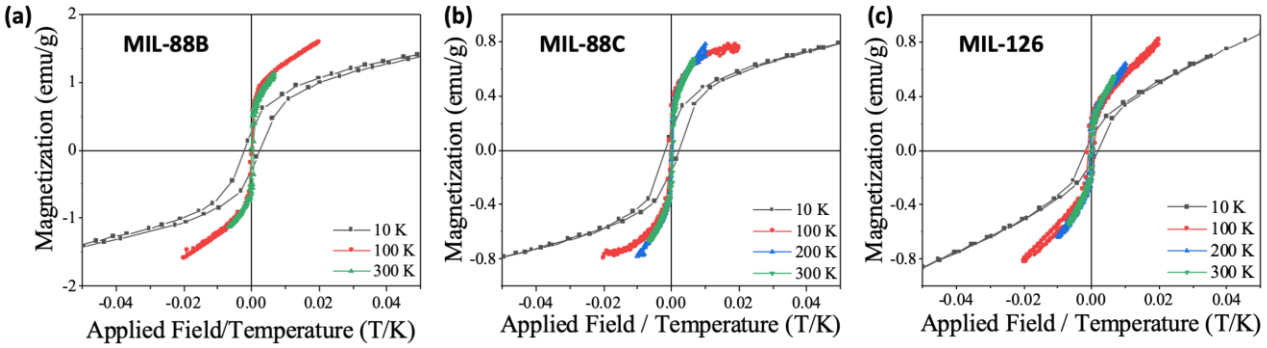

Figure 6. M-H/T loops for (a) MIL-88B, (b) MIL-88C, and (c) MIL-126.

ARTICLE

Table 2 summarizes the nanocrystals' lattice parameters (cell length and crystal volume) and E_α calculated for each MIL-88 analogue. The thermal energies are calculated using Eq. 2 at 100 K, 200 K, and 300 K and are 8.62 x 10^{-3} eV, 1.72 x 10^{-2} eV, and 2.5 x 10^{-2} eV, respectively. All three MIL-88 analogues exhibit very small anisotropy energies, which are below the thermal energies calculated for the selected temperature range of 100 to 300 K. The theoretical calculations also predict that all three MOFs could show superparamagnetic response in the temperature range of 100 to 300 K. The M-H plots were recorded at four intermediate temperatures between 10 K and 300 K for MIL-88(Fe)-MOFs. **Figure 6** represents the respective M-H plots where *x*-axis represents normalized applied field with respect to the temperature. The purpose of this normalization is to demonstrate the superparamagnetic nature of the MOF samples above their respective blocking temperatures.[69,70] The M-H/T plots are superimposed to one another, evidencing the superparamagnetic state of all three samples in the temperature range of 100 to 300 K.[69,70] The experimental results agree with the theoretical prediction and confirm that the shape anisotropy and finite-size of nanocrystals contributes to lowering the magnetic anisotropy energy at $T>T_B$, resulting in superparamagnetic behaviour in all three MIL-88(Fe) analogues.

In response to the superparamagnetic behavior in MIL-88 analogues at the temperature range of 100 to 300 K, the smaller size nanocrystals contribute to two key intrinsic material's characteristics – magnetic anisotropy and Curie temperature (T_C). When the particle size is smaller anisotropy becomes less stable and leads to disorder in magnetic moments. This leads to the thermal energy overpasses the anisotropy energy of the particles at higher temperature ($T>T_B$), generating the superparamagnetic state of randomly arranged spins.[71–73] On the other hand, when the particle size becomes really small, the fluctuations of electron spins become more prominent, which results in drastic decrease in the T_C of the material, causing magnetic moments to change direction randomly and thus creates disorder, exhibiting superparamagnetic state.[71–73] Since MIL-88(Fe)-MOFs show short range order superparamagnetic response at a higher temperature range, including the room temperature (300 K), it is an indicative of that MIL-88 analogues' T_C are above the room temperature. Thus, our findings suggests that the superparamagnetic response in MIL-88 is due to their finite size effect and the shape anisotropy, acting nanocrystals as single nanodomains within the MOF microstructure.

Despite the nanocrystal size and shape anisotropy, Fe_3O clusters, themselves also could act as single-magnetic domains within the framework due to the isoreticular expansion of the MIL-88 framework. The length of the organic linker and its effective conjugation length play a key role in the electron density on the metal oxide nodes.[74] Typically, most MOFs are insulators due to the lack of effective overlap between d-orbitals of the metal node and ligand's p_z orbitals, resulting in localized electron density on the metal oxide nodes instead of delocalization through organic linker units.[75] This could create isolated metal oxide clusters with localized electron spin densities, which can act as a single-magnetic domain in the crystal lattice of MOF. Also, electron density distribution can reveal if there is a magnetic cooperativity from the organic linker to induce the long-range magnetic order. If the electron densities and spin density of states are localized within the Fe_3O domains, there is no extended magnetic cooperativity from the ligands and short-range order of magnetic moment changes corresponds to localized spin density resided on Fe_3O clusters.

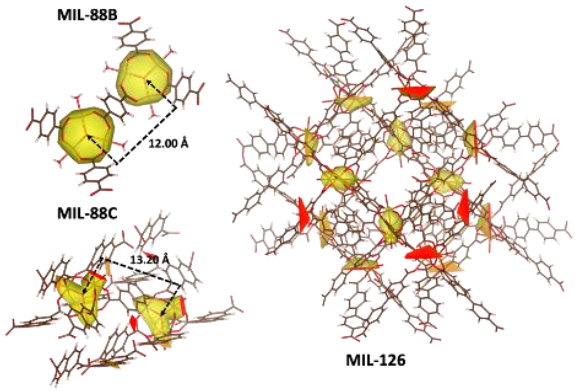

Figure 7. Electron density distribution maps of MIL-88(Fe)-MOFs.

To go deeper in understanding of the synergistic effect of the isoreticular framework expansion and the electron density distribution of metal oxide clusters and the electron spin density state on the magnetic ordering of MIL-88(Fe)-MOFs, we modelled the electronic density distributions of Fe_3O units using VESTA and spin densities of each model unit using Gaussian 16 at the UB3LYP/6-31G(d) theoretical level. As depicted in **Figure 7**, all three MOFs exhibit localized electron density (**LED**) around Fe_3O clusters, revealing that there is no delocalization of electron density through organic likers. This also reveals that there is no effect of the increasing the effective conjugation length for the magnetic ordering, suggesting that organic ligands in the framework are more less likely to induce the magnetic cooperativity. Thus, it is clear that magnetic response in MOFs is contributed by the **LED** of Fe_3O clusters in the crystal lattices of all three MIL-88 analogues. The model systems with the highest spin multiplicity from all three

MIL-88 analogue's monomeric units were constructed and the subsequent spin density distributions were shown at the isovalue 0.002 electrons/Å^3. As shown in **Figure 8**, reduced models were built with a linker molecule (dianion) bonding to two Fe_3O domains in its two ends. Each Fe_3O domain includes five formate anions and three water molecules, securing an octahedral coordination for each iron ion and charge neutrality for the whole model system. With two Fe^{3+} and one Fe^{2+} ions in each Fe_3O domain, the total unpaired electrons reach 14 and the spin multiplicity for each whole reduced model is thus 29. Results show that the spin density in all cases is localized on each Fe_3O center and there is spin density extends to the carboxylate groups, which bind to irons. But there is no observable delocalization over the linker molecules. Therefore, owing to the short-range ordering of magnetic moments within Fe_3O domains, MIL-88 analogues function as a molecular-based ferromagnet at 10 K and a molecular-based superparamagnetic at 100 to 300 K. The isoreticular nature of the organic linkers are contributed to the expansion of the framework, thereby tailoring the size, shape, and nanocrystal volume.

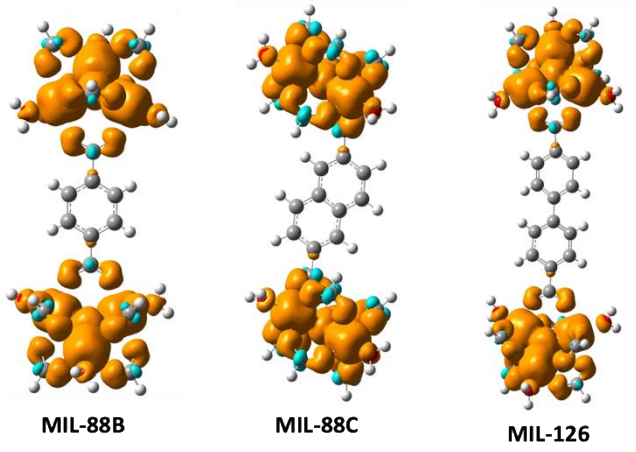

Figure 8. Computed electron spin density distribution of each MIL-88 analogue modelled unit at the UB3LYP/6-31G(d) theoretical level with the isovalue 0.002 e/Å^3.

To this end, we have conducted the preliminary investigation on the magnetic response of isoreticular MIL-88(Fe)-MOFs. Our studies demonstrate that magnetic behaviour of all three MIL-88 analogues is independent from the linker length and its effective conjugation. But isoreticular framework expansion has allowed us to tailor the finite size and shape anisotropy of nanocrystals of each MIL-88 analogue's microstructures, exhibiting ferromagnetism at $T<T_B$ and superparamagnetism at $T>T_B$, respectively. Although there are no prior experimental studies reported on the size and shape anisotropy dependent magnetic response in any type of MOFs nanocrystals, our findings agree with the previous studies on the particle-size and shape dependence of Fe_3O_4 nanoparticles.[61,62] Additionally, at this stage we have not conducted further studies to understand the nature of phase transition from ferromagnetic state to superparamagnetic state. But our electron density and spin density distributions in the models suggest that Fe_3O clusters in each MIL-88 nanocrystal's lattice act as localized single magnetic domains, which contribute to spin density, magnetic ordering, and the spin transition to generate ferromagnetic state at low temperature and superparamagnetic state at a certain temperature range, including room temperature. Further theoretical explanation and experimental investigation are still required and will aid to understand the interactions among the nanocrystals with respect to the temperature, thereby will allow to elucidate the temperature dependent effective superparamagnetic moment (μ_{SP}) at room temperature and above.

Experimental

Materials: Terephthalic acid (1,4-benzene dicarboxylic acid, BDC), 2,6-naphthalene dicarboxylic acid (NDC), 4,4'-biphenyl dicarboxylic acid (BPDC), and N,N-dimethylformamide (DMF) were purchased from Sigma Aldrich. Iron(II)acetate anhydride was purchased from STREM Chemicals. Chloroform (HPLC Grade) was purchased from Fisher Chemicals. All the solvents and reagents were used as received.

Characterization: The elemental analysis, chemical bonding environments, and elemental oxidation states of synthesized MIL-88(Fe)-MOFs were obtained from X-ray photoelectron spectroscope (XPS-Escalab Xi+-Thermos Scientific). The Fourier transform infrared spectra (FT-IR Varian 670-IR spectrometer) were recorded in the range of 500-4000 cm^{-1} to analyze the chemical composition and functional groups. The powder diffraction patterns for all three MIL-88 MOFs were obtained using X ray- powder diffractometer (XRD, Agilent technologies Gemini), using Cu source at K_α wavelength. VESTA (Version 3.3.4, 64-bit edition) was used for the visualization of Fe^{III}-MOFs' crystal structures from their respective cif files, acquired from Cambridge Crystallographic Data Center (CCDC) and Crystallography Open Database (COD). The surface area and pore volume of synthesized MOFs were obtained using micrometric analyzer. The N_2 adsorption-desorption isotherms measured at 77 K after degassing of samples at 1500C for 6 hours. Thermogravimetric analysis (Model - Q500) was conducted under nitrogen atmosphere heating the samples up to 7000C at the increment of 100C/ min to determine the thermal stability of MOFs. A scanning electron microscope (Zeiss Auriga FIB/FESEM) was used to image the surface morphologies of MOFs and transmission electron microscopy (Libra 120 kV and HR-TEM JEOL2100 PLUS with STEM/EDS capability) was used to analyze the nanodomains' intrinsic morphologies and size distribution, and crystallinity with lattice spacing of the three MOFs. The Magnetic properties were measured using Vibrating sample magnetometer (VSM) an integral part of Quantum Design Physical property measurement system (PPMS).

Synthesis of MIL-88 B, C and MIL-126: Following the previously published procedure,[36] MIL-88B, MIL88-C, and MIL-88D were prepared from their respective organic linkers and iron(II)acetate. In a typical procedure, the organic linker (50 mg, 0.2 mmol) and Iron (II)acetate (78 mg, 0.4 mmol) were added to

anhydrous DMF solution (2 mL). The reactants were stirred for 15 minutes at room temperature prior to heating to 260 °C for 7 minutes. The resulting pinkish powder were collected by centrifugation and immediately washed with cold DMF to remove unreacted ligands. The powdered samples were then washed with de-ionized water thrice. Finally, the sample was dried under vacuum at 100 °C for 12 hours before characterization. FT-IR stretching (cm^{-1}): MIL-88B - 3294 (broad OH), 1646 (carboxylate carbonyl), 1497-1584 (aromatic C=C bonds), and 1377 (C-O-Fe); MIL-88C - 3457 (broad OH), 1661 (carboxylate carbonyl), 1586-1600 (aromatic C=C bonds), and 1419 (C-O-Fe); and MIL-126 - 3500 (broad OH), 1670 (carboxylate carbonyl), 1605 (aromatic C=C bonds), and 1400-1355 (C-O-Fe). Elemental analysis (%weight): MIL-88B with formula of $Fe_3O(BDC)_3$ – Found: C (41.41), O (32.73), Fe (24.77); Theoretical: C (41.54), O (32.28), Fe (24.14); MIL-88C with formula of $Fe_3O(NDC)_3$ – Found: C (50.89), O (27.05), Fe (20.17); Theoretical: C (50.86), O (26.35), Fe (19.71); MIL-126 with formula of $Fe_3O(BPDC)_3$ – Found: C (53.89), O (24.90), Fe (18.95); Theoretical: C (54.70), O (24.29), Fe (18.17); XPS survey analysis along with elemental compositions and binding energies of each elements for all three MIL-88 analogues are listed in Table S1.

N_2-desoprtion isotherms: Brunner-Emmett-Teller (BET) method was used to determine the pore size, pore volume and the surface area of the products. For this purpose, the samples obtained were activated for BET analysis by soaking the samples in chloroform for three consecutive days by replacing with fresh chloroform for every 6 hours. Prior to measurements the samples were dried under vacuum at 80°C for 3 hours followed by degassing of samples at 150°C for 12 hours. In BET analysis, the surface area was calculated based on the equation obtained from adsorption isotherm in the relative pressure range of P/P_0 = 0.07-0.3. The information about the pore size distribution was derived from N_2 desorption isotherms using Barret-Joyner-Halenda (BJH) plots. Further, the total volume of product per gram was determined from the amount of N_2 adsorbed at P/P_0=1.

Magnetic measurements: The magnetic properties of MOF samples were measured using the vibrating sample magnetometer in a Quantum Design Physical Property Measurements System (PPMS). A known amount of the powder samples was filled in non-magnetic sample holders supplied by the Quantum Design. The magnetization measurements of the powder samples were carried out using the QD vibrating sample magnetometer (VSM) option in the physical property measurement system (PPMS). The VSM option for the PPMS consists of a VSM linear motor head for vibrating the sample, a coil-set puck for detection, and electronics for driving the linear motor and detecting the response from the pick coils. The magnetization measurement was accomplished by oscillating the sample (amplitude 1-3 mm and at frequency 40 Hz) near a detection coil and synchronously detecting the voltage induced. The system is cable of resolving the magnetization changes of less than 10^{-6} emu at a data rate of 1 Hz. The M-H measurements were carried out at multiple temperatures ranging from 10 K to 300 K. The M-T measurements entailed zero field cooled (ZFC) process where the sample was cooled from room temperature to 10 K in zero field and then a magnetic field of 200 G was applied. The magnetization was recorded while warming up of the samples from 10 K to 300 K.

Computational Analysis: Electron density distribution within the lattice for Fe_3O clusters were modeled from VESTA (3.5.7 version) which uses the Fourier transform of structure factors that are calculated from structure parameters and atomic scattering factors of free atoms.[76] The spin densities were performed at the UB3LYP/6-31G(d) theoretical level with Gaussian 16.

Conclusions

In summary, we have synthesized porous microstructures of isoreticular MIL-88(Fe)-MOFs and investigated their magnetic properties for low-density molecular-based magnets. Three MIL-88 analogues; MIL-88B, MIL-88C, and MIL-126 were synthesized by a solvent-driven self-assembly-based solvothermal method to yield the MIL-88 topology, i.e, **6-connected acs** net, with the empirical formula of $Fe_3O(L)_3$. The porosity, crystal structure and packing, unit cell volume, crystal size, and shape anisotropy were elucidated to understand their magnetic response. The magnetic properties, studied by acquiring the M-T and M-H curves, have provided evidence of nano-crystalline size and shape anisotropy dependent magnetic phase transitions from ferromagnetism at low temperature (10 K) to superparamagnetic at room temperature (from 100 to 300 K). The electron density distributions on Fe_3O clusters, modelled using VESTA, and spin densities modelled using Gaussian 16 have revealed the magnetic ordering in the framework, confirming that magnetic response is induced strictly by the localized electron density and spin density of state on Fe_3O domains. Therefore, isoreticulation has no effect on the magnetic response and there is no evidence of long-range ordering through magnetic cooperativity from the ligands. However, isoreticular expansion impacts on the nanocrystals size and their ordered assembly within the microstructure. Nanocrystals act as single-magnetic domains with superparamagnetic size threshold to induce the short-range ordering of phase transition from ferromagnetism to superparamagnetism. Thus, this principles study provides an insight into how one can create low-density molecular-based magnets using the size and shape-controlled MOFs nanocrystals.

Author Contributions

The manuscript was written through contributions of all authors. All authors have given approval to the final version of the manuscript.

Conflicts of interest

There are no conflicts to declare.

Acknowledgements

This work is performed at the Joint School of Nanoscience and Nanoengineering, a member of the South-eastern Nano-technology Infrastructure Corridor (SENIC) and National Nanotechnology Coordinated Infrastructure (NNCI), sup-ported by the NSF (Grant ECCS-1542174). Financial support for this work is provided, in part, from the Joint School of Nanoscience and Nanoengineering and the Office of Re-search, University of North Carolina at Greensboro. Authors also acknowledge the DOD HBCU/MSI instrumentation award (Contract #: W911NF1910522) to acquire HR-TEM (JEOL 2100PLUS) with STEM/EDS capability. Authors gratefully acknowledge Dhananjay Kumar from Mechanical Engineering Department at North Carolina A&T University, for his guidance provided for magnetization experiments.

References

1 S. Bedanta, A. Barman, W. Kleemann, O. Petracic and T. Seki, A Subject for Both Fundamental Research and Applications, *J. Nanomater.*, 2013, 1–22.
2 E. Coronado, Molecular Magnetism: From Chemical Design to Spin Control in Molecules, Materials and Devices, *Nat. Rev. Mater.*, 2020, **5**, 87–104.
3 L. Bogani and W. Wernsdorfer, Molecular Spintronics Using Single-Molecule Magnets. In Nanoscience and technology: a collection of reviews from nature journals; World Scientific, 2010, 194–201.
4 J. Camarero and E. Coronado, Inorganic Spintronics: The Role of Molecular Materials and Single Molecules. *J. Mater. Chem.*, 2009, **19**, 1678–1684.
5 S. Sanvito, Molecular Spintronics, *Chem. Soc. Rev.*, 2011, **40**, 3336–3355.
6 D. Maspoch, D. Ruiz-Molina and J. Veciana, Magnetic Nanoporous Coordination Polymers, *J. Mater. Chem.*, 2004, **14**, 2713–2723.
7 D. Maspoch, D. Ruiz-Molina and J. Veciana, Old Materials with New Tricks: Multifunctional Open-Framework Materials, *Chem. Soc. Rev.*, 2007, **36**, 770–818.
8 R. J. Kuppler, D. J. Timmons, Q.-R. Fang, J.-R. Li, T. A. Makal, M. D. Young, D. Yuan, D. Zhao, W. Zhuang and H.-C. Zhou, Potential Applications of Metal-Organic Frameworks, *Coord. Chem. Rev.*, 2009, **253**, 3042–3066.
9 P. Dechambenoit and J. R. Long, Microporous Magnets, *Chem. Soc. Rev.*, 2011, **40**(6), 3249–3265.
10 E. Coronado and G. M. Espallargas, Dynamic Magnetic MOFs, *Chem. Soc. Rev.*, 2013, **42**, 1525–1539.
11 L. Li, G. J. Clarkson, D. J. Evans, M. R. Lees, S. S. Turner and P. Scott, Isomeric Fe (II) MOFs: From a Diamond-Framework Spin-Crossover Material to a 2D Hard Magnet, *Chem. Commun.*, 2011, **47**, 12646–12648.
12 M.-S. Chen, W. Li, M.-B. Zhang, R.-X. Hu, C.-H. Zhang and Z.-M. Chen, Structure and Magnetic Properties of a Three-Dimensional Cobalt Metal-Organic Framework, *Z. Für Naturforschung B*, 2011, **66**, 1175–1178.
13 X.-L. Tong, T.-L. Hu, J.-P. Zhao, Y.-K. Wang, H. Zhang and X.-H. Bu, Chiral Magnetic Metal–Organic Frameworks of MnII with Achiral Tetrazolate-Based Ligands by Spontaneous Resolution, *Chem. Commun.*, 2010, **46**, 8543–8545.
14 D. W. Ryu, W. R. Lee, J. W. Lee, J. H. Yoon, H. C. Kim, E. K. Koh and C. S. Hong, Magnetic Metal–Organic Framework Constructed from a Paramagnetic Metalloligand Exhibiting a Significant Sorption and Reversible Magnetic Conversions, *Chem. Commun.*, 2010, **46**, 8779–8781.
15 P. Mahata, D. Sarma and S. Natarajan, Magnetic Behaviour in Metal-Organic Frameworks—Some Recent Examples, *J. Chem. Sci.*, 2010, **122**, 19–35.
16 M. Kurmoo, Magnetic Metal–Organic Frameworks,*Chem Soc Rev*, 2009, **38**, 1353–1379.
17 E. D. Bloch, W. L. Queen, R. Krishna, J. M. Zadrozny, C. M. Brown and J. R. Long, Hydrocarbon Separations in a Metal-Organic Framework with Open Iron (II) Coordination Sites, *science*, 2012, **335**, 1606–1610.
18 L. Shen, S.-W. Yang, S. Xiang, T. Liu, B. Zhao, M.-F. Ng, J. Göettlicher, J. Yi, S. Li and L. Wang, Origin of Long-Range Ferromagnetic Ordering in Metal–Organic Frameworks with Antiferromagnetic Dimeric-Cu (II) Building Units, *J. Am. Chem. Soc.*, 2012, **134**, 17286–17290.
19 A. D. Katsenis, E. K. Brechin and G. S. Papaefstathiou, Metal-Organic Frameworks: Derived from Single Molecule Magnets. In Encyclopedia of Inorganic and Bioinorganic Chemistry, ed. R. A. Scott, John Wiley & Sons, Ltd, Chichester, UK, 2014, pp. 1–14.
20 R. Dong, Z. Zhang, D. C. Tranca, S. Zhou, M. Wang, P. Adler, Z. Liao, F. Liu, Y. Sun and W. Shi, A Coronene-Based Semiconducting Two-Dimensional Metal-Organic Framework with Ferromagnetic Behavior, *Nat. Commun.*, 2018, **9**, 1–9.
21 C. Yang, R. Dong, M. Wang, P. S. Petkov, Z. Zhang, M. Wang, P. Han, M. Ballabio, S. A. Bräuninger and Z. Liao, A Semiconducting Layered Metal-Organic Framework Magnet, *Nat. Commun.*, 2019, **10**, 1–9.
22 B. Li, H.-M. Wen, W. Zhou and B. Chen, Porous Metal–Organic Frameworks for Gas Storage and Separation: What, How, and Why? , *J. Phys. Chem. Lett.*, 2014, **5**, 3468–3479.
23 Y. Li and R. T. Yang, Gas Adsorption and Storage in Metal–Organic Framework MOF-177, *Langmuir*, 2007, **23**, 12937–12944.
24 H.-C. Zhou, J. R. Long and O. M. Yaghi, Introduction to Metal–Organic Frameworks, *Chem. Rev.*, 2012, **112**, 673–674.
25 V. R. Cherkasov, E. N. Mochalova, A. V. Babenyshev, J. M. Rozenberg, I. L. Sokolov and M. P. Nikitin, Antibody-Directed Metal-Organic Framework Nanoparticles for Targeted Drug Delivery, Acta *Biomater.*, 2020, **103**, 223–236.
26 J. Cao, X. Li and H. Tian, Metal-Organic Framework (MOF)-Based Drug Delivery, Curr. *Med. Chem.*, 2020, **27**, 5949–5969.
27 W. Liu, Y. Zhong, X. Wang, C. Zhuang, J. Chen, D. Liu, W. Xiao, Y. Pan, J. Huang and J. Liu, A Porous Cu (II)-Based Metal-Organic Framework Carrier for PH-Controlled Anticancer Drug Delivery, *Inorg. Chem. Commun.*, 2020, **111**, 107675.
28 M. D. Allendorf, C. A. Bauer, R. K. Bhakta and R. J. T. Houk, Luminescent Metal–Organic Frameworks, *Chem. Soc. Rev.*, 2009, **38**, 1330–1352.
29 M. Pamei and A. Puzari, A. Luminescent Transition Metal–Organic Frameworks: An Emerging Sensor for Detecting Biologically Essential Metal Ions, *Nano-Struct. Nano-Objects*, 2019, **19**, 100364.
30 H. Xu, F. Liu, Y. Cui, B. Chen and G. Qian, A Luminescent Nanoscale Metal–Organic Framework for Sensing of Nitroaromatic Explosives, *Chem. Commun.*, 2011, **47**, 3153.
31 C.-S. Liu, J. Li and H. Pang, Metal-Organic Framework-Based Materials as an Emerging Platform for Advanced Electrochemical Sensing, *Coord. Chem. Rev.*, 2020, **410**, 213222.

32 G. M. Espallargas and E. Coronado, Magnetic Functionalities in MOFs: From the Framework to the Pore, *Chem. Soc. Rev.*, 2018, **47**, 533–557.
33 A. E. Thorarinsdottir and T. D. Harris, Metal–Organic Framework Magnets, Chem. *Rev.*, 2020, **120**, 8716–8789.
34 I.-R. Jeon, B. Negru, R. P. Van Duyne and T. D. Harris, A 2D Semiquinone Radical-Containing Microporous Magnet with Solvent-Induced Switching from T C= 26 to 80 K, *J. Am. Chem. Soc.*, 2015, **137**, 15699–15702.
35 M. A. Halcrow, Ed., *Spin-crossover materials: properties and applications*, Wiley, Chichester, West Sussex, United Kingdom, 2013.
36 S. Dawood, R. Yarbrough, K. Davis and H. Rathnayake, Self-Assembly and Optoelectronic Properties of Isoreticular MOF Nanocrystals, *Synth. Met.*, 2019, **252**, 107–112.
37 S. Dawood, A. Dorris, K. Davis, N. I. Hammer and H. Rathnayake, Synthesis, Characterization, and Photophysics of Self-Assembled Mn (II)-MOF with Naphthalene Chromophore, *J. Phys. Chem. C*, 2021, **125**, 792–802.
38 C. Serre, F. Millange, S. Surblé and G. Férey, A Route to the Synthesis of Trivalent Transition-Metal Porous Carboxylates with Trimeric Secondary Building Units, *Angew. Chem. Int. Ed.*, 2004, **43**, 6285–6289.
39 S. A. Orefuwa, H. Yang and A. J. Goudy, Rapid Solvothermal Synthesis of an Isoreticular Metal–Organic Framework with Permanent Porosity for Hydrogen Storage, *Microporous Mesoporous Mater.*, 2012, **153**, 88–93.
40 M. Ma, A. Bétard, I. Weber, N. S. Al-Hokbany, R. A. Fischer and N. Metzler-Nolte, Iron-Based Metal–Organic Frameworks MIL-88B and NH2-MIL-88B: High Quality Microwave Synthesis and Solvent-Induced Lattice "Breathing.", *Cryst. Growth Des.*, 2013, **13**, 2286–2291.
41 T. Yamashita and P. Hayes, Analysis of XPS Spectra of Fe2+ and Fe3+ Ions in Oxide Materials, *Appl. Surf. Sci.*, 2008, **254**, 2441–2449.
42 A. G. Kolhatkar, A. C. Jamison, D. Litvinov, R. C. Willson and T. R. Lee, Tuning the Magnetic Properties of Nanoparticles, *Int. J. Mol. Sci.*, 2013, **14**, 15977–16009.
43 Y. Wu, H. Luo and H. Wang, Synthesis of Iron (III)-Based Metal–Organic Framework/Graphene Oxide Composites with Increased Photocatalytic Performance for Dye Degradation, *RSC Adv.*, 2014, **4**, 40435–40438.
44 Y.-S. Wei, M. Zhang, P.-Q. Liao, R.-B. Lin, T.-Y. Li, G. Shao, J.-P. Zhang and X.-M. Chen, Coordination Templated [2+ 2+ 2] Cyclotrimerization in a Porous Coordination Framework, Nat. *Commun.*, 2015, **6**, 1–7.
45 D. Dubbeldam, *MIL-88C-dry.cif*.
46 C. Serre, C. Mellot-Draznieks, S. Surble, N. Audebrand, Y. Filinchuk and G. Ferey, Role of Solvent-Host Interactions That Lead to Very Large Swelling of Hybrid Frameworks, *Science*, 2007, **315**, 1828–1831.
47 D. Dubbeldam, *MIL-88C-open.cif*.
48 M. Dan-Hardi, H. Chevreau, T. Devic, P. Horcajada, G. Maurin, G. Férey, D. Popov, C. Riekel, S. Wuttke and J.-C. Lavalley, How Interpenetration Ensures Rigidity and Permanent Porosity in a Highly Flexible Hybrid Solid, *Chem. Mater.*, 2012, **24**, 2486–2492.
49 I. A. Baburin, V. A. Blatov, L. Carlucci, G. Ciani and D. M. Proserpio, Interpenetrating Metal-Organic and Inorganic 3D Networks: A Computer-Aided Systematic Investigation. Part II [1]. Analysis of the Inorganic Crystal Structure Database (ICSD), *Reticular Chem. Des. Synth. Prop. Appl. Met.-Org. Polyhedra Framew.*, 2005, **178**, 2452–2474.
50 O. Delgado Friedrichs, M. O'Keeffe and O. M. Yaghi, Three-Periodic Nets and Tilings: Regular and Quasiregular Nets, *Acta Crystallogr. A.*, 2003, **59**, 22–27.
51 K. S. W. Sing, Reporting Physisorption Data for Gas/Solid Systems with Special Reference to the Determination of Surface Area and Porosity (Provisional), *Pure Appl. Chem.*, 1982, **54**, 2201–2218.
52 M. Ahmad, X. Quan, S. Chen and H. Yu, Tuning Lewis Acidity of MIL-88B-Fe with Mix-Valence Coordinatively Unsaturated Iron Centers on Ultrathin Ti3C2 Nanosheets for Efficient Photo-Fenton Reaction, *Appl. Catal. B Environ.*, 2020, **264**, 118534.
53 S. K. Maji, N. Mukherjee, A. Mondal and B. Adhikary, Synthesis, Characterization and Photocatalytic Activity of α-Fe2O3 Nanoparticles, *Polyhedron.*, 2012, **33**, 145–149.
54 M.-H. Pham, G.-T. Vuong, A.-T. Vu and T.-O, Novel Route to Size-Controlled Fe–MIL-88B–NH 2 Metal–Organic Framework Nanocrystals, *Langmuir.*, 2011, **27**, 15261–15267.
55 T. Rijnaarts, R. Mejia-Ariza, R. J. M. Egberink, W. van Roosmalen and J. Huskens, Metal-Organic Frameworks (MOFs) as Multivalent Materials: Size Control and Surface Functionalization by Monovalent Capping Ligands*, Chem. - Eur. J.*, 2015, **21**, 10296–10301.
56 D. Bara, C. Wilson, M. Mörtel, M. M. Khusniyarov, S. Ling, B. Slater, S. Sproules and R. S. Forgan, Kinetic Control of Interpenetration in Fe–Biphenyl-4, 4'-Dicarboxylate Metal–Organic Frameworks by Coordination and Oxidation Modulation, *J. Am. Chem. Soc.*, 2019, **141**, 8346-8357
57 S. Shaji, N. R. Mucha, P. Giri, C. Binek and D. Kumar, Magnetic and Magnetocaloric Properties of Fe2Ta Thin Films, *AIP Adv.*, 2020, **10**, 025222.
58 D. Kumar, H. Zhou, T. K. Nath, A. V. Kvit, J. Narayan, V. Craciun and R. K. Singh, Improved Magnetic Properties of Self-Assembled Epitaxial Nickel Nanocrystallites in Thin-Film Ceramic Matrix, *J. Mater. Res.,* 2002, **17**, 738–742.
59 N. B. Herndon, S. H. Oh, J. T. Abiade, D. Pai, J. Sankar, S. J. Pennycook and D. Kumar, Effect of Spacer Layer Thickness on Magnetic Interactions in Self-Assembled Single Domain Iron Nanoparticles, *J. Appl. Phys.*, 2008, **103**, 07D515.
60 J. T. Abiade, S. H. Oh, D. Kumar, M. Varela, S. Pennycook, H. Guo, A. Gupta and J. Sankar, The Effect of Matrix and Substrate on the Coercivity and Blocking Temperature of Self-Assembled Ni Nanoparticles*, J. Appl. Phys.*, 2008, **104**, 073910.
61 U. Meisen and H. Kathrein, The Influence of Particle Size, Shape and Particle Size Distribution on Properties of Magnetites for the Production of Toners*, J. Imaging Sci. Technol.*, 2000, **44**, 508–513.
62 Q. Li, C. W. Kartikowati, S. Horie, T. Ogi, T. Iwaki and K. Okuyama, Correlation between Particle Size/Domain Structure and Magnetic Properties of Highly Crystalline Fe3O4 Nanoparticles, *Sci. Rep.*, 2017, **7**, 1–7.
63 J. Frenkel and J. Doefman, Spontaneous and Induced Magnetisation in Ferromagnetic Bodies, *Nature.*, 1930, **126**, 274–275.
64 C. Kittel, Theory of the Structure of Ferromagnetic Domains in Films and Small Particles, Phys. Rev., 1946, **70**, 965–971.
65 S. Mørup, M. F. Hansen and C. Frandsen, 1.04 Magnetic Nanoparticles, *Compr. Nanosci. Nanotechnol. Elsevier Amst. Neth.*, 2019, 89–140.
66 C. P. Bean and J. D. Livingston, Superparamagnetism, *J. Appl. Phys.*, 1959, **30**, S120–S129.

67 S. Bedanta and W. Kleemann, Supermagnetism, *J. Phys. Appl. Phys.*, 2009, **42**, 013001.
68 B. D. Cullity and C. D. Graham, Introduction to magnetic materials, IEEE/Wiley, Hoboken, N.J, 2nd ed., 2009.
69 J. T. Abiade, G. X. Miao, A. Gupta, A. A. Gapud and D. Kumar, Structural and Magnetic Properties of Self-Assembled Nickel Nanoparticles in a Yttria Stabilized Zirconia Matrix*, Thin Solid Films*, 2008, **516**, 2082–2086.
70 D. Kumar, S. Yarmolenko, J. Sankar, J. Narayan, H. Zhou and A. Tiwari, Pulsed Laser Deposition Assisted Novel Synthesis of Self-Assembled Magnetic Nanoparticles, *Compos. Part B Eng.,* 2004, **35**, 149–155.
71 R. H. Kodama, A. E. Berkowitz, E. J. McNiff, Jr. and S. Foner, Surface Spin Disorder in NiFe2O4 Nanoparticles, *Phys. Rev. Lett.,* 1996, **77**, 394–397.
72 D. Lin, A. C. Nunes, C. F. Majkrzak and A. E. Berkowitz, Polarized Neutron Study of the Magnetization Density Distribution within a CoFe2O4 Colloidal Particle II, *J. Magn. Magn. Mater.,* 1995, **145**, 343–348.
73 J. Jiang, G. F. Goya and H. Rechenberg, Magnetic Properties of Nanostructured CuFe2O4, *J. Phys.: Condens.* Matter., 1999, **11**, 4063–4078.
74 H. Rathnayake, S. Saha, S. Dawood, S. Loeffler and J. Starobin, Analytical Approach to Screen Semiconducting MOFs Using Bloch Mode Analysis and Spectroscopic Measurements, *J. Phys. Chem. Lett.,* 2021, **12**, 884–891.
75 A. A. Talin, A. Centrone, A. C. Ford, M. E. Foster, V. Stavila, P. Haney, R. A. Kinney, V. Szalai, F. El Gabaly and H. P. Yoon, Tunable Electrical Conductivity in Metal-Organic Framework Thin-Film Devices, *science.*, 2014, **343**, 66–69.
76 D. Waasmaier and A. Kirfel, *Acta Crystallogr., Sect. A: Found. Crystallogr.,* 1995, **51**, 416-418.